Type-II Dirac surface states in topological crystalline insulators

Ching-Kai Chiu,[1,2,3] Y.-H. Chan,[4] Xiao Li,[3] Y. Nohara,[5] and A. P. Schnyder[5]

[1]*Department of Physics and Astronomy, University of British Columbia, Vancouver, BC, Canada V6T 1Z1*
[2]*Quantum Matter Institute, University of British Columbia, Vancouver BC, Canada V6T 1Z4*
[3]*Condensed Matter Theory Center and Joint Quantum Institute and Maryland Q Station, Department of Physics,*
University of Maryland, College Park, Maryland 20742, USA
[4]*Institute of Atomic and Molecular Sciences, Academia Sinica, Taipei 10617, Taiwan*
[5]*Max-Planck-Institute for Solid State Research, Heisenbergstr. 1, D-70569 Stuttgart, Germany*

Recently, it has been realized that topological Weyl semimetals come in two different varieties: (i) with standard Weyl cones with pointlike Fermi surfaces (type I) and (ii) with tilted Weyl cones that appear at the contact of electron and hole pockets (type II). These two types of Weyl semimetals have very different physical properties, in particular, in their thermodynamics and magnetotransport. Here, we show that Dirac cone surface states of topological *crystalline* insulators can be distinguished in a similar way. We demonstrate this in terms of a general surface theory and then apply this knowledge to a family of antiperovskites of the form A_3EO, where A denotes an alkaline earth metal, while E stands for Pb or Sn. Using *ab initio* DFT calculations, we investigate the bulk and surface topology of these antiperovskites and show that they exhibit type-I as well as type-II Dirac surface states protected by reflection symmetry. We find that the type-II Dirac states, as opposed to the type-I Dirac states, exhibit characteristic van Hove singularities in their dispersion, which lead to different thermodynamic properties, and which can serve as an experimental fingerprint of type-II surface states. The different magnetotransport characteristics between type-I and type-II surface states are discussed. In addition, we show that both type-I and type-II surface states exhibit an unusual helical spin polarization, which could lead to topological surface superconductivity.

I. INTRODUCTION

Topological crystalline insulators (TCIs) are insulating in the bulk, but exhibit conducting boundary states protected by crystal symmetries [1–4]. As opposed to surface states of ordinary insulators, the gapless modes at the surface of TCIs arise due to a nontrivial topology of the bulk wave functions, which is characterized by a quantized topological invariant, e.g., a mirror Chern or mirror winding number [4–10]. One prominent example of a TCI is the rocksalt semiconductor SnTe [10–13], which supports at its (001) surface four Dirac cones protected by reflection symmetries. The surface modes of this and all other known TCIs are of the standard Dirac fermion type with closed pointlike (or circular) Fermi surfaces, which we refer to as "type I". However, as we discuss in this article, *crystal* symmetries can also give rise to new types of surface fermions, namely type-II Dirac surface states, which are tilted Dirac cones that appear at the touching of electron and hole pockets [14]. This distinction between type-I and type-II cones is analogous to the type-I and type-II Weyl semimetals [15–19], which have recently been predicted to exist in WTe$_2$ [15] and LaAlGe [20]. Similar to the type-II Weyl semimetals, we find that type-II Dirac surface states exhibit thermodynamic and magnetotransport properties that are markedly different from their type-I counterparts.

In this paper, we first show in terms of a general surface theory that type-II Dirac cones can exist on the surface of topological *crystalline* insulators [4–10], which is in contrast to ordinary topological insulators, where they are forbidden by symmetry. Secondly, we predict that the antiperovskites A_3EO [21–26] (where A denotes an alkaline earth metal, while E stands for Pb or Sn) are an example of a topological

crystalline insulator that hosts this new type of Dirac cone at its surface. Using first-principles calculations and a tight-binding model, we perform a systematic study of the surface states of A_3EO, with a particular focus on Ca$_3$PbO, which crystallizes in its low-temperature phase in the cubic space group $Pm\bar{3}m$. We find that the (011) surface exhibits type-II Dirac nodes, whereas the (111) surface supports both type-I and type-II Dirac states. On the (001) surface, on the other hand, the Dirac nodes overlap with the bulk bands. All these surface states are protected by the crystal symmetries of A_3EO, in particular the reflection symmetries. We show that the type-II Dirac nodes, in contrast to type-I Dirac states, exhibit characteristic van Hove singularities in their dispersions, which lead to different thermodynamic properties and which can be used as an experimental fingerprint. Moreover, we find that the magnetotransport properties are different between type-I and type-II Dirac states. In particular, we show how the Landau level spectra of type-II Dirac nodes radically differ from those of type-I Dirac states. For type-II Dirac nodes, the zeroth Landau level unpins from the energy of the Dirac band crossing. Finally, we uncover the unique helical spin texture of the type-I and type-II surface states, which could lead to exotic surface superconductivity. Indeed, as was recently shown [27], the antiperovskites A_3EO become bulk superconducting upon hole doping. Hence a topological superconducting phase in the surface states of A_3EO can be proximity induced by the bulk superconductivity.

The remainder of the this paper is organized as follows. In Sec. II, we show, in terms of a generic low-energy theory, that crystalline topological insulators can host both type-I and type-II Dirac surface states. We compare the two-dimensional type-II surface states to the recently discussed type-II Weyl cones of
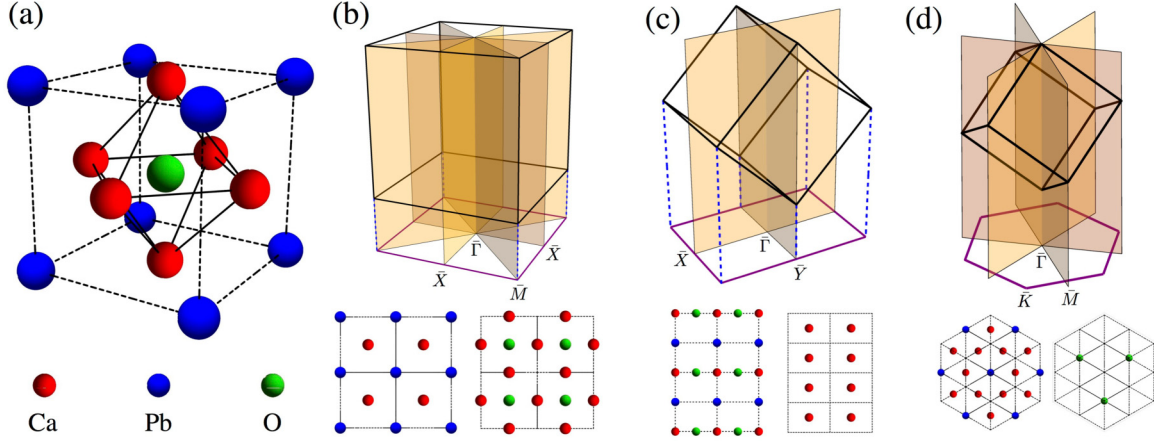
FIG. 1. Crystal symmetries and surface terminations. (a) Crystal structure of Ca_3PbO. (b), (c), and (d) Surface Brillouin zones (BZs) for the (001), (011), and (111) surfaces, respectively. For the (001) and (011) surfaces, the surface BZs can be obtained from the bulk cubic BZs by projecting along the [001] and [011] directions, respectively. For the (111) surface BZ, this is not possible. Nevertheless, the symmetries of the surface BZ follow from the projection of the bulk reflection planes [see (d)]. The brown shaded areas in (b), (c), and (d) indicate the bulk mirror planes. The lower panels show the different surface terminations. The crystal symmetries of the (001), (011), and (111) surfaces are described by the 2D space groups $p4m$, pmm, and $p3m1$, respectively.

three-dimensional semimetals. In Sec. III, we predict that the antiperovskites A_3EO host the type-II states on their surfaces. We compute the dispersion and spin polarization of these Dirac surface states (Sec. III B) and derive the topological invariants that protect them (Sec. III A). Section III C is devoted to the study of the Landau level spectra of the type-II surface states. Our conclusions and outlook are given in Sec. IV.

II. TYPES OF 2D SURFACE FERMIONS

Before considering the detailed topology of the antiper-ovskites A_3EO, let us first present a general discussion of the types of fermions that can arise at the surface of topological (crystalline) insulators. The Hamiltonian describing the low-energy physics of two-dimensional (2D) surface Dirac states is of the generic form [28]

$$H_{\text{surf}}(\mathbf{k}) = \sum_{\substack{i=1,2 \\ \alpha=0,1,2}} k_i A_{i\alpha} \sigma_\alpha, \qquad (2.1)$$

where k_i denote the two surface momenta, σ_i are the Pauli matrices, and σ_0 represents the 2×2 identity matrix. Here, we have kept terms only up to linear order in k_i. The energy spectrum of H_{surf} is given by

$$E_\pm = \sum_i k_i A_{i0} \pm \sqrt{\sum_j \left(\sum_i k_i A_{ij} \right)^2} \equiv L(\mathbf{k}) \pm W(\mathbf{k}), \qquad (2.2)$$

where the sums are over $i, j = 1, 2$. The second term $W(\mathbf{k})$ in Eq. (2.2) is the linear spectrum of standard (i.e., type-I) Dirac fermions. That is, for $L(\mathbf{k}) < W(\mathbf{k})$, the surface state is categorized as type I. Since the energy of type-I Dirac states is dispersive in all directions, we require that $\det(A_{ij}) \neq 0$. On the other hand, if there exists one momentum direction $\mathbf{k}_0$, such that $L(\mathbf{k}_0) > W(\mathbf{k}_0)$, we categorize the surface state as type II. This is in analogy to the three-dimensional (3D) type-II Weyl points, which have been recently discovered in $WeTe_2$ [15]. We

note that, while 3D Weyl points are stable in the absence of any symmetry (except translation), two-dimensional surface Dirac states can only exist in the presence of time-reversal symmetry or spatial symmetries, such as reflection.

Now, the interesting question is how these symmetries restrict the form of Eq. (2.1). For a 3D time-reversal (TR) invariant strong topological insulator, the Hamiltonian H_{STI} satisfies $T H_{\text{STI}}(-\mathbf{k}) T^{-1} = H_{\text{STI}}(\mathbf{k})$, with the time-reversal operator $T = \sigma_y K$ and the complex conjugation operator K. This symmetry locks the Dirac node at the time-reversal invariant points of the BZ, such as, e.g., $\mathbf{k} = 0$. We observe that the linear term $k_i \sigma_0$ is forbidden by time-reversal symmetry. Hence the surface states of TR invariant strong topological insulators are described by

$$H_{\text{STI}}^{\text{surf}}(\mathbf{k}) = k_y \sigma_x - k_x \sigma_y, \qquad (2.3)$$

and are therefore always of type I.

However, type-II Dirac fermions can appear at the surface of reflection symmetric TCIs (and weak TR symmetric topological insulators). The reflection symmetric Hamiltonian

TABLE I. Family of antiperovskite materials with cubic space group $Pm\bar{3}m$. The tolerance (tol.) factor indicates the deviation from the ideal inverse perovskite structure [25]. The bulk gap values are obtained from *ab initio* first principles calculation. The wave-function topology is determined by the mirror Chern numbers C_{x^0}, C_{x^π}, and $C_{x,y}$ (see Appendix A). We find that the topology is nontrivial, with $C_{x^0} = C_{x,y} = 2$ and $C_{x^\pi} = 0$, for all compounds except for Ba_3SnO.

	tol. factor	bulk gap	topology
Ca_3PbO	0.999	~15 meV	nontrivial
Ca_3SnO	0.993	~5 meV	nontrivial
Sr_3PbO	0.978	~18 meV	nontrivial
Sr_3SnO	0.973	~7 meV	nontrivial
Ba_3PbO	0.962	~10 meV	nontrivial
Ba_3SnO	0.957	gapless	–

of these type-II surface states is generically given by

$$H_{\text{TCI}}^{\text{surf}}(k_x,k_y) = Ak_y\sigma_0 + k_y\sigma_x - k_x\sigma_y, \qquad (2.4)$$

with $A > 1$. (Without loss of generality we have set the Fermi velocities to 1 and assumed that the reflection plane is $k_x = 0$.) The type-II Dirac state (2.4) is protected by reflection symmetry $x \to -x$, which acts on (2.4) as

$$R_x H_{\text{TCI}}^{\text{surf}}(-k_x,k_y)R_x^{-1} = H_{\text{TCI}}^{\text{surf}}(k_x,k_y), \qquad (2.5)$$

with the reflection operator $R_x = \sigma_x$. Since reflection flips the sign of k_x, it allows the linear term $Ak_y\sigma_0$ but forbids $k_x\sigma_0$.

The crucial difference between type-I and type-II Dirac surface states is that the former have closed circular Fermi surfaces, whereas the latter exhibit open electron and hole pockets which touch each other. As one varies the Fermi energy E_F, the Fermi surface of type-I Dirac states can be shrunk to a single point, which is called a type-I Dirac point. In contrast, type-II Dirac states give rise to electron and hole pockets, whose size depends on the Fermi energy. At a certain E_F the electron and hole Fermi surfaces touch each other, which is called a type-II Dirac point. As opposed to type-I Dirac points, the density of states at type-II Dirac points remains finite. In addition, we observe that in type-II Dirac states one of the two surface bands must bend over in order to connect bulk valence and conduction bands. As a consequence, there is a maximum in the dispersion of the surface states. The latter gives rise to a van Hove singularity, which leads to a kink in the surface density of states. This can be used as an experimental fingerprint of type-II Dirac states.

III. TOPOLOGY OF ANTIPEROVSKITE MATERIALS

As an example of a TCI with type-II Dirac surface states, we consider the cubic antiperovskite materials A_3EO with space group $Pm\bar{3}m$ (Table I). The crystal structure of A_3EO is an inverse perovskite structure, where the oxygen atom O is surrounded octahedrally by the alkaline earth metal atoms A [see Fig. 1(a)]. We choose Ca_3PbO as a generic representative of this materials class. The bulk band structure of Ca_3PbO displays six Dirac cones, which are gapped by spin-orbit coupling (Table I). While Ca_3PbO is known to be a trivial TR invariant insulator [22] (i.e., a trivial class AII insulator [4]), it has recently been argued that reflection symmetries give rise to a nontrivial wave-function topology with nonzero mirror Chern numbers [26].

A. Nontrivial topology

Let us now discuss in detail how the nontrivial topology of A_3EO arises due to reflection symmetry. First, we observe that the space group $Pm\bar{3}m$ possesses nine different reflection symmetries R_i which transform $\mathbf{r} = (x,y,z)$ as (see Fig. 1)

$$R_x\mathbf{r} = (-x,y,z), \qquad R_{y,\pm z}\mathbf{r} = (x,\pm z,\pm y), \qquad (3.1a)$$

$$R_y\mathbf{r} = (x,-y,z), \qquad R_{z,\pm x}\mathbf{r} = (\pm z,y,\pm x), \qquad (3.1b)$$

$$R_z\mathbf{r} = (x,y,-z), \qquad R_{x,\pm y}\mathbf{r} = (\pm y,\pm x,z). \qquad (3.1c)$$

By Fourier transforming into momentum space, we find that there are 12 mirror planes in the Brillouin zone (BZ), namely, $k_i = 0,\pi$ and $k_i = \pm k_j$ for $i,j = x$, y, z and $i \neq j$. For each of these reflection planes we can define a mirror Chern number [7,8,29]. However, due to the cubic rotational symmetries, only 3 out of these 12 mirror invariants are independent. Without loss of generality, we choose as an independent set the mirror Chern numbers C_{x^0}, C_{x^π}, and $C_{x,y}$ that are defined for the reflection planes $k_x = 0$, π, and k_y, respectively. Considerations based on first-principles derived tight-binding models show that for the cubic antiperovskites the mirror Chern numbers take the values $C_{x^0} = C_{x,y} = 2$ and $C_{x^\pi} = 0$ (see Appendix A, Appendix B, and Table I). Thus in total there are nine nonzero mirror Chern numbers, i.e., $C_{i^0} = C_{i,\pm j} = 2$ for $i,j = x,y,z$ and $i \neq j$. The mirror Chern numbers can also be derived from a low-energy effective theory. As shown in Appendix C, the low-energy description of A_3EO is given by six gapped Dirac cones. Within this low-energy model one finds that there exists only one bulk gap term m, which respects the reflection symmetries and which gaps out all six Dirac cones. The sign of this gap opening term, $\text{sgn}(m)$, determines the mirror Chern numbers, i.e.,

$$C_{x,y} = \text{sgn}(m) + b_{x,y}, \quad C_{x^0} = 2\,\text{sgn}(m) + b_x, \quad (3.2)$$

where $b_{x,y}$ and b_x are the mirror Chern numbers of the "background" bands, i.e., those filled bands that are not included in the low-energy description of the bulk Dirac cones. For the cubic antiperovskites, we find that $b_{x,y} = 1$ and $b_x = 0$. Hence C_{x^0} is always nonzero even if the sign of the gap term switches.

B. Surface states

By the bulk-boundary correspondence, a nontrivial value of the mirror Chern numbers C_{i^0} (or $C_{i,\pm j}$) leads to the
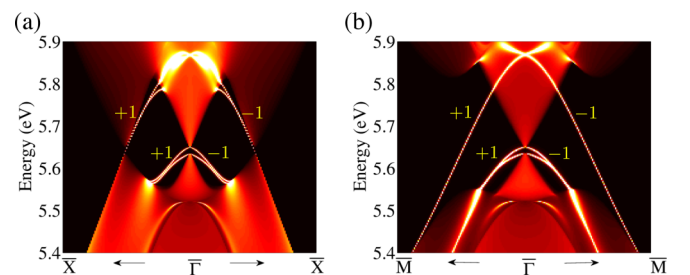
FIG. 2. Density of states at the (001) surface. (a) and (b) Surface density of states along the high-symmetry lines $\bar{\Gamma} \to \bar{X}$ and $\bar{\Gamma} \to \bar{M}$ of the (001) surface BZ, respectively, for the Pb-Ca termination [lower left panel in Fig. 1(b)]. The two high-symmetry directions correspond to the two inequivalent mirror lines of Fig. 1(b), i.e., $k_y = 0$ and $k_x = k_y$. The spectrum along the mirror line $k_y = 0$ [see panel (a)] exhibits two right-moving chiral modes with mirror eigenvalue $R_y = +1$ and two left-moving chiral modes with mirror eigenvalue $R_y = -1$. Similarly, the spectrum along the mirror line $k_y = k_x$ [see panel (b)] shows two right-moving chiral modes with $R_{x,-y} = +1$ and two left-moving chiral modes with $R_{x,-y} = -1$. We observe that the Dirac nodal points (i.e., the band crossings) for the upper chiral modes are hidden by the bulk bands. For the lower chiral modes, there is no band crossing at all, since the modes are too far apart.

appearance of Dirac states on those surfaces that are left invariant by the corresponding mirror symmetry R_{i^0} (or $R_{i,\pm j}$). That is, the value of C_{i^0} (or $C_{i,\pm j}$) indicates the number of left- and right-moving chiral modes in the surface BZ. These chiral surface modes are located within the mirror line $k_i = 0$ (or $k_i = \pm k_j$), which is symmetric under the reflection operation R_{i^0} (or $R_{i,\pm j}$), see Fig. 1. Importantly, left- and right-moving surface chiral modes belong to opposite eigenspaces of the reflection operators R_{i^0} (or $R_{i,\pm j}$), and therefore cannot hybridize, see Fig. 2. That is, the band crossing between the left- and right-moving modes is protected by reflection symmetry. Depending on the surface orientation of A_3EO, this band crossing corresponds to the Dirac point of a type-I surface state, the touching of electron- and hole-pockets of a type-II Dirac state, or is completely hidden in the bulk bands. In the following, we discuss these three possibilities for the case of Ca$_3$PbO.

1. Hidden Dirac nodes on the (001) surface

We start by examining the Dirac states on the (001) surface for the Ca-Pb termination [lower left panel in Fig. 1(b)]. Projecting the symmetries of $Pm\bar{3}m$ along the (001) direction, one finds that the two-dimensional space group of the (001) surface is $p4m$ [30]. The wallpaper group $p4m$ contains

four reflection symmetries, i.e., R_x, R_y, $R_{x,+y}$, and $R_{x,-y}$ [Fig. 1(b)]. In the surface BZ, this gives rise to six mirror lines $k_x = 0, k_x = \pi, k_y = 0, k_y = \pi, k_x = \pm k_y$ with three independent mirror Chern numbers C_{x^0}, C_{x^π}, and $C_{x,y}$. From the above analysis we find that $C_{x^0} = C_{y^0} = 2$ and $C_{x,y} = C_{x,-y} = 2$, which leads to two pairs of left- and right-moving chiral modes within the mirror lines $k_x = 0$, $k_y = 0$ and $k_x = +k_y$, $k_x = -k_y$, respectively. The left- and right-moving chiral modes belong to reflection eigenspaces with $R = -1$ and $R = +1$, respectively. This is clearly visible in Fig. 2, which shows the surface density of states along the high-symmetry lines $\bar{\Gamma} \to \bar{X}$ and $\bar{\Gamma} \to \bar{M}$, which correspond to the mirror lines $k_x = 0$ and k_y, respectively. Interestingly, the band crossing formed by the upper left- and right-moving chiral modes is completely hidden by the bulk bands. The lower chiral modes, on the other hand, do not show a band crossing, since they are too far apart. Similar chiral modes also appear for the Ca-O termination, see Fig. 10 in Appendix E.

2. Type-II Dirac nodes on the (011) surface

Next, we consider the Dirac states on the (011) surface, whose wallpaper group is pmm. We focus here on the Ca-Pb-O termination; the results for the other termination are shown in Appendix E. The two-dimensional space group
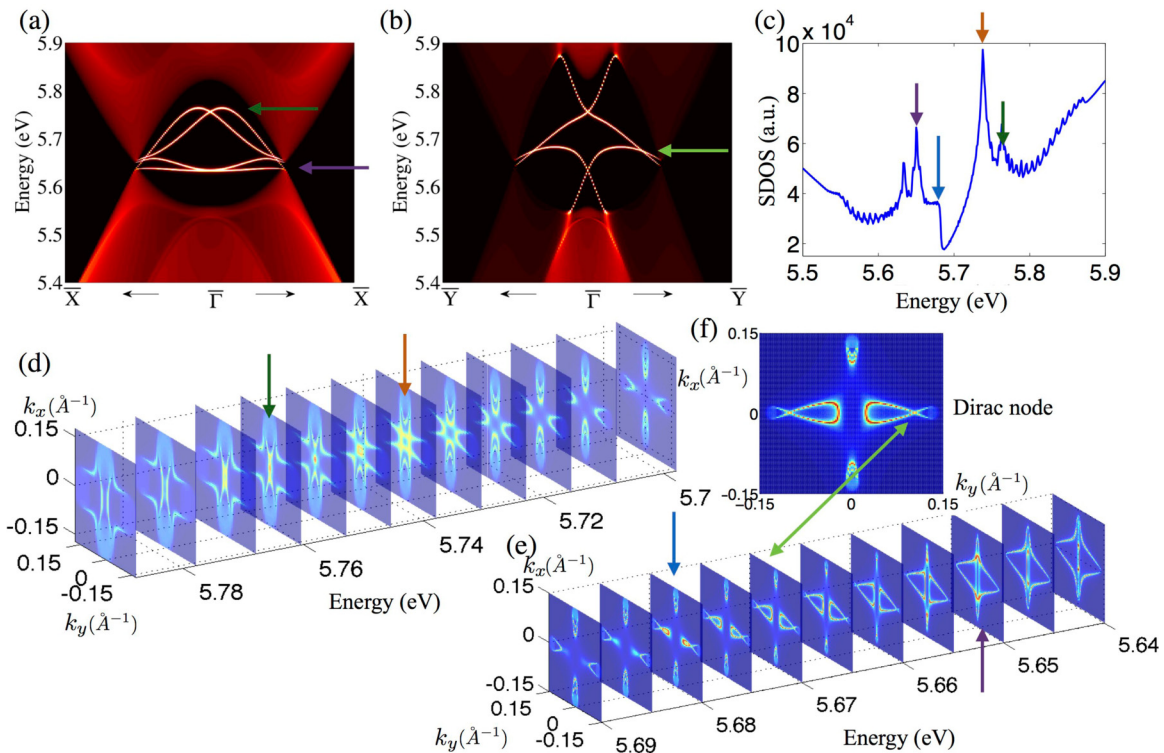
FIG. 3. Density of states at the (011) surface. (a) and (b) Surface density of states along the high-symmetry lines $\bar{\Gamma} \to \bar{X}$ and $\bar{\Gamma} \to \bar{Y}$ of the (011) surface BZ, respectively, for the Ca-Pb-O termination [lower left panel in Fig. 1(c)]. The two high-symmetry lines represent the intersection of the (011) surface plane with the mirror planes $k_x = 0$ and $k_y = k_z$ of Fig. 1(c). The corresponding mirror symmetries protect the surface band crossings that are visible in (a) and (b). (c) shows the energy resolved surface density of states, which exhibits several van Hove singularities as indicated by the green, orange, blue, and purple arrows. (d) and (e) display the energy- and momentum-resolved surface density of states for different energy ranges. The van Hove singularities are marked by the arrows, except for the light green one, which indicates the touching of electron and hole pockets. (f) shows the momentum-resolved surface density of states at the energy of the type-II Dirac point, which is marked by the light green arrow.

pmm contains two reflection symmetries, R_x and $R_{y,z}$, see Fig. 1(c). Correspondingly, the (011) surface BZ exhibits two mirror lines, namely, $k_x = 0$ and $k_y = k_z$, with the two nonzero mirror Chern numbers C_{x^0} and C_{yz}. Since $C_{x^0} = C_{yz} = 2$, there appear two pairs of left- and right-moving chiral surface modes within the mirror lines $k_x = 0$ and $k_y = k_z$, see Fig. 3. Hybridization between the left- and right-moving chiral modes is prohibited, since they belong to different eigenspaces of the reflection operators. As indicated by the light green arrows in Figs. 3(b), 3(f), and 3(e), the two chiral modes at the (011) surface cross each other at $E = 5.67$ eV and form a type-II Dirac point. In the close vicinity of this type-II Dirac point, the velocity of the two chiral modes has the same sign. However, one of the two surface modes needs to bend over in order to connect bulk valence and conduction bands. This leads to a maximum and therefore a van Hove singularity in the dispersion of the surface modes. The latter reveals itself in the surface density of states as a kink at $E = 5.68$ eV, see blue arrows in Figs. 3(c) and 3(e). This feature in the surface density of states can be used as an experimental fingerprint of the type-II Dirac state. Another key feature of type-II Dirac points is the touching of electron and hole pockets, see light green arrow at $E = 5.67$ eV in Figs. 3(e) and 3(f).

Besides the type-II Dirac nodes at $E = 5.67$ eV, there are also two accidental band crossings at the $\bar{\Gamma}$ point of surface BZ. These band crossings can be removed by an

adiabatic deformation of the surface states. Associated with these accidental Dirac nodes are three van Hove singularities. First, the band crossing at $E = 5.75$ eV realizes a van Hoves singularity, which leads to a divergence in the density of states [orange arrow in Figs. 3(c) and 3(d)]. Second, the maximum at $E = 5.76$ eV in the dispersion of the surface states gives rise to a kink in the surface density of states [dark green arrow in Figs. 3(a) and 3(c)]. Third, the flat dispersion of the surface states near $E = 5.65$ eV leads to a peak in the density of states [violet arrow in Figs. 3(a), 3(c), and 3(e)].

3. Type-I and type-II Dirac nodes on the (111) surface

Finally, we examine the Dirac states on the (111) surface for the Ca-Pb termination. (We note that the surface states of the O termination are expected to be similar to the ones of the Ca-Pb termination, since the oxygen bands are far away in energy from the Fermi energy.) Projecting the three-dimensional space group $Pm\bar{3}m$ along the (111) direction, we find that the wallpaper group for the (111) surface is $p3m1$. The two-dimensional space group $p3m1$ contains three reflection symmetries, i.e., $R_{x,y}$, $R_{x,z}$, and $R_{y,z}$. The corresponding mirror lines in the surface BZ are $k_x = k_y$, $k_x = k_z$, and $k_y = k_z$, i.e., the $\bar{M}$-$\bar{\Gamma}$-$\bar{M}$ lines. For each of the three mirror lines one can define a mirror Chern number $C_{i,j}$, which are related to each other by the threefold rotation symmetries of $Pm\bar{3}m$. As
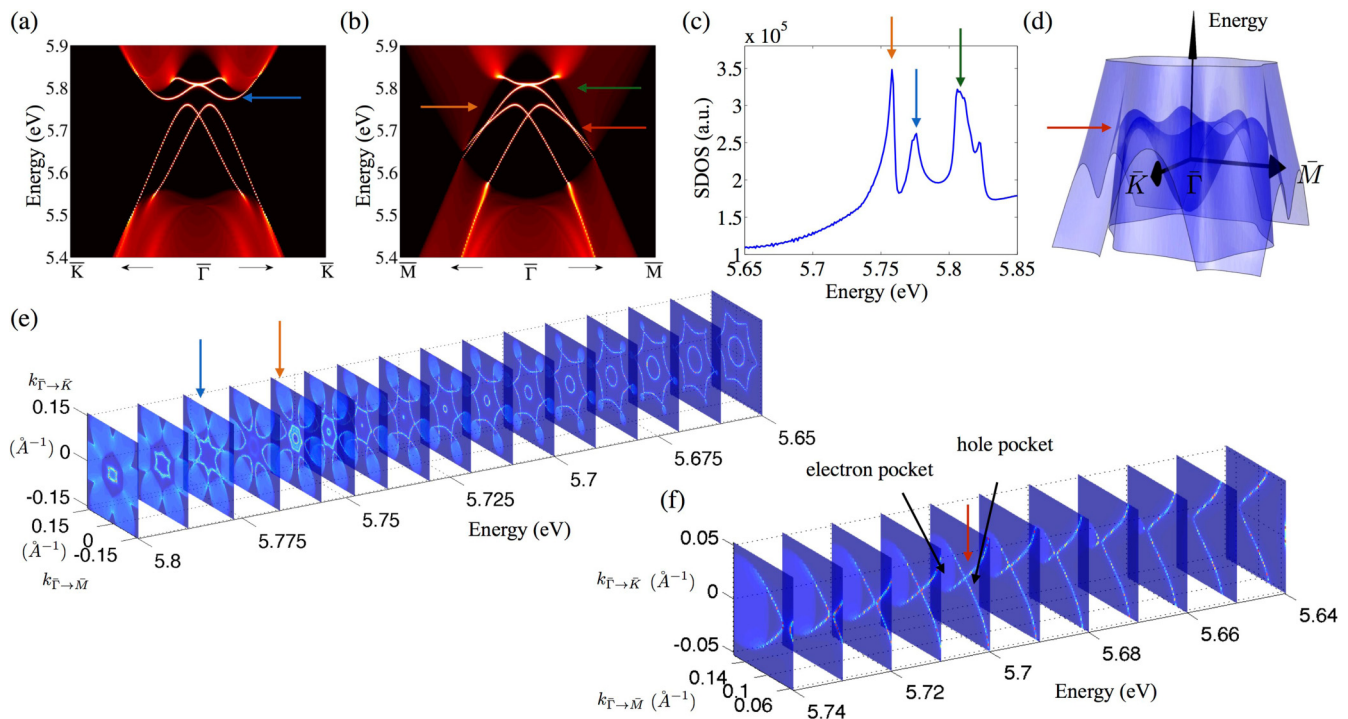
FIG. 4. Density of states at the (111) surface. (a) and (b) Surface density of states along the high-symmetry lines $\bar{\Gamma} \to \bar{K}$ and $\bar{\Gamma} \to \bar{M}$ of the (111) surface BZ, respectively, for the Ca-Pb termination. The $\bar{\Gamma} \to \bar{M}$ direction corresponds to the mirror lines of the (111) surface. Thus the spectrum along $\bar{\Gamma} \to \bar{M}$ is gapless and there appear two type-II Dirac states protected by reflection symmetry. The spectrum along the $\bar{\Gamma}$-$\bar{K}$ line, on the other hand, is gapped, since it is not a mirror line. (c) Surface density of states which exhibits several van Hove singularities as indicated by the orange, blue, and green arrows. The van Hove singularity at $E = 5.76$ eV (orange peak) stems from the back bending of the type-II Dirac state. (d) Schematic illustration of the six type-II Dirac states on the (111) surface. (e) and (f) Energy- and momentum-resolved surface density of states for different energy ranges. The van Hove singularities are indicated by the blue and orange arrows. The red arrow indicates the type-II Dirac point at $E = 5.70$ eV, where the electron and hole pockets meet.

discussed in Sec. III A, we find that $C_{x,y} = C_{x,z} = C_{y,z} = 2$. By the bulk-boundary correspondence, it follows that there appear two pairs of left- and right-moving chiral modes within the $\bar{M} - \bar{\Gamma} - \bar{M}$ lines of the surface BZ, see Fig. 4(b). These chiral bands cross each other at $E = 5.70$ eV, thereby forming type-II Dirac points [red arrow in Fig. 4(b)]. Close to these type-II Dirac points, the velocities of the chiral modes have the same sign. But further away, one of the two modes bends over, such that it connects bulk valence and conduction bands. Hence this surface band must exhibit a maximum [orange arrows in Figs. 4(b) and 4(e)], which leads to a van Hove singularity in the surface density of states at $E = 5.76$ eV [orange arrow in Fig. 4(c)]. Another key feature of this type-II Dirac state is the touching of the electron and hole Fermi surfaces. That is, with increasing Fermi energy the open electron and hole pockets approach each other, touch at the type-II Dirac point with $E = 5.70$ eV [red arrow in Fig. 4(f)], and then separate again.

In addition to these type-II Dirac nodes, the (111) surface also exhibits two accidental type-I Dirac nodes at the $\bar{\Gamma}$ point, which can be removed by adiabatic transformations. Connected to these accidental Dirac nodes are two van Hove singularities. First, the Dirac point at $E = 5.81$ eV represents a saddle-point van Hove singularity, which leads to a log divergence in the surface density of states [green arrows in Figs. 4(b) and 4(c)]. Second, the lower bands of the Dirac state at $E = 5.81$ eV bend over, forming a minimum at $E = 5.78$ eV. This leads to a kink in the surface density of states [blue arrow in Figs. 4(a) and 4(c)].

4. Spin polarization of surface states

The surface states of the antiperovskites A_3EO are all singly degenerated and therefore exhibit a helical spin texture. We demonstrate this in Fig. 5 for the (001) surface with Ca-Pb termination (compare also with Fig. 2). Due to spin-orbit coupling the spin orientations of both Dirac surface states are locked to their momenta, i.e., the Dirac states exhibit a helical spin texture. We find that the spin of the surface state is polarized entirely within the surface plane, at all energies. Interestingly, the helicity of the outer Dirac state is opposite to the one of the inner Dirac state, see Fig. 5(a). As was shown recently [27], A_3EO becomes a bulk superconductor upon
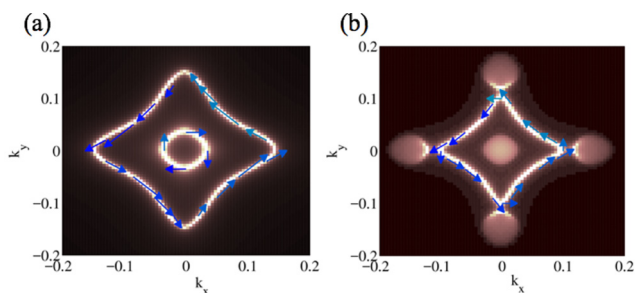
FIG. 5. Spin polarization of the Dirac states at the (001) surface. (a) and (b) Momentum-resolved surface density of states and spin polarization for the (001) face (Ca-Pb termination) at the energies $E = 5.60$ and 5.67 eV, respectively. The spin polarization, which is purely in-plane, is indicated by the arrows. The direction of the spin polarization is correlated with the momentum, forming a 90° angle.

hole doping, which in turn might induced a superconducting phase in the surface states. Note that, because of the helical spin texture, the proximity-induced surface topological phase is most likely topological. If so, and if additional symmetries are preserved, the vortices of the surface superconductor are expected to host zero-energy Majorana modes [31].

C. Landau level spectrum

A drastic difference between type-I and type-II Dirac surface states arises when a magnetic field is applied. For type-I Dirac cones the energy spectrum of the Landau levels is given by

$$E_n \sim \sqrt{n}, \qquad (3.3)$$

where n is the Landau level index. Hence, the Landau levels of type-I Dirac cones are in general well separated. This is in contrast to type-II Dirac cones. To illustrate this, let us consider the following tight-binding model on a square lattice [32],

$$H = -\sum_{\langle ij \rangle} t_{ij} b_j^\dagger a_i + t_1 \sum_{\langle ij \rangle} (a_j^\dagger a_i + b_j^\dagger b_i), \qquad (3.4)$$

where a_i and b_i denote the electron annihilation operators on the sublattice A and B, respectively. t_{ij} represent the nearest-neighbor hopping, while t_1 is the next-nearest-neighbor hopping integral (for more details see Appendix D). Hamiltonian (3.4) describes two Dirac cones, whose tilting is controlled by the ratio t_1/t, with $t = |t_{ij}|$. For $t_1/t = 0$, there is no tilting [Fig. 6(a)] and for $t_1/t = 0.2$ there is a small tilting [Fig. 6(b)]. In both cases there exist well separated Landau levels. (Note that the dispersive curves in the Landau level structure are due to edge states and therefore should be ignored in the following discussion.) At $t_1/t = 1/2$, there is a transition from type-I Dirac states to type-II Dirac states. At this transition point the spectrum becomes nondispersive along the k_2 direction and the Landau levels get very dense around $E = 0$ (i.e., around the energy of the Dirac point) [Fig. 6(c)]. Finally, for $t_1/t > 1/2$, there appear type-II Dirac cones with open electron and hole pockets. As shown in Fig. 6(d), for type-II Dirac cones the separation between the Landau levels near $E = 0$ is close to zero, leading to a sizable region of very dense Landau levels [cf. Fig. 6(d)]. This region of dense Landau levels arises because the open electron and hole Fermi surfaces enclose a very large momentum-space area, which is much larger than the one enclosed by type-I Dirac states (for a detailed explanation, see Appendix D). Moreover, we find that for type-II Dirac states the zeroth Landau level E_0 of the type-I Dirac node [see Figs. 6(a) and 6(b)] becomes unpinned and moves away from $E = 0$.

IV. DISCUSSION

Using general symmetry arguments, we have shown that the surface of crystalline topological insulators can host type-II Dirac surface states, which are characterized by open electron and hole Fermi surfaces that touch each other. This is in contrast to regular strong topological insulators, where the Dirac surface states, due to time-reversal symmetry, are always of type-I, which exhibit a closed small Fermi surface. By means of a DFT-derived tight-binding model and a low-energy
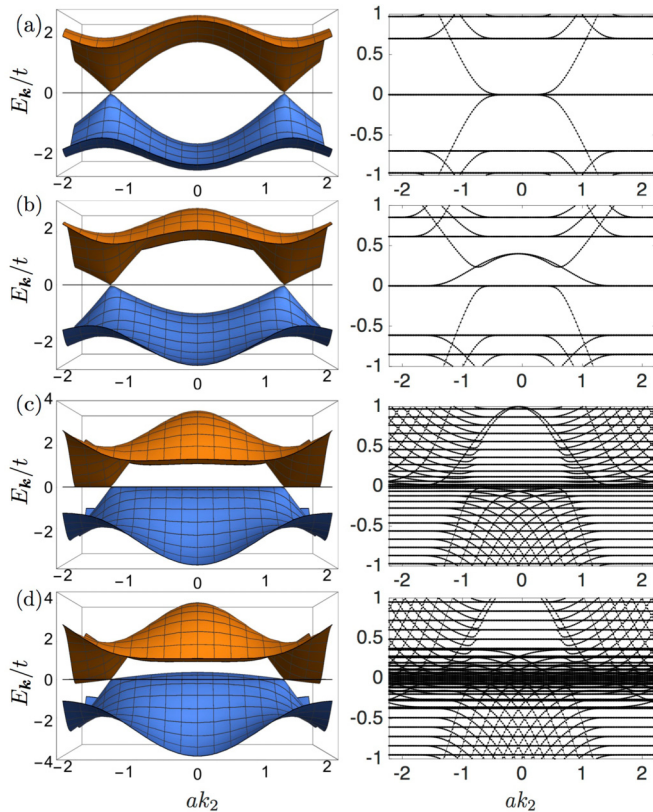
FIG. 6. Landau level spectrum for type-I and type-II Dirac surface states. The left and right columns show the energy spectrum and Landau level structure, respectively, for the tight-binding model given by Eq. (3.4). The magnetic field strength is chosen to be $B = 0.01\phi_0/a^2$, where $\phi_0 \equiv h/e$ is the flux quantum and a^2 is the area of a plaquette of the square lattice, see Fig. 8. The tilting of the Dirac cones is controlled by the ratio t_1/t. The four rows correspond to (a) $t_1/t = 0$ (type-I Dirac cone), (b) $t_1/t = 0.2$ (type-I Dirac cone), (c) $t_1/t = 0.5$ (transition between type-I and -II Dirac cones), and (d) $t_1/t = 0.6$ (type-II Dirac cone), respectively. All dispersive curves in the Landau level structure arise from states localized at the edge of the sample, and thus are not of interest here.

theory, we have predicted that type-II Dirac states appear at the surfaces of the cubic antiperovskite materials A_3EO.

For these cubic antiperovskites, which exhibit two independent reflection symmetries, we have computed the mirror Chern numbers and shown that they are equal to two for the $k_i = 0$ and $k_i = \pm k_j$ (for $i,j = x,\ y,\ z$ and $i \neq j$) mirror planes, indicating that there appear two left- and right-moving modes on surfaces that are invariant under the mirror symmetries. Depending on the surface orientation and termination these left- and right-moving modes form type-I or type-II Dirac nodes, or do not cross at all. We remark that while the mirror Chern numbers determine the number of left- and right-moving chiral modes that connect valence and conduction bands, they do not give any information about the type and the number of band crossings in the surface spectrum. This is because, (i) the Dirac points might be hidden in the bulk, (ii) the left- and right-moving modes might be too far apart to form a crossing, or (iii) there might be additional accidental band crossings.

We have investigated in detail the physical properties of the type-II surface states that distinguish them from their type-I counterparts. One characteristic feature of type-II Dirac states are their van Hove singularities, which arise because one of the two chiral modes needs to bend over in order to connect valence with conduction bands. These van Hove singularities lead to divergences and kinks in the surface density of states, which can serve as unique fingerprints of the type-II Dirac states. Another distinguishing feature of type-II Dirac states is their Landau level spectrum. As opposed to type-I Dirac states, where the Landau levels are well separated, for type-II Dirac states there exists a very large density of Landau levels near the band-crossing energy (see Fig. 6). Moreover, for type-II Dirac states the zeroth Landau level becomes unpinned from the energy of the Dirac node. In addition, we have uncovered the helical spin texture of the Dirac surface states (see Fig. 5). Due to this spin texture, it might be possible to proximity induce a topological superconducting phase on the surface. In particular, since the antiperovskites become bulk superconductors upon doping [27], they might therefore be an ideal platform for studying topological surface superconductivity. It will be interesting to compare the above mentioned theoretical predictions with future quantum oscillation, angle-resolved photoemission, and scanning tunneling experiments.

APPENDIX A: DFT CALCULATIONS AND TOPOLOGICAL INVARIANTS

In this appendix, we give some details about our *ab initio* band structure calculations and describe how the topological invariants are computed.

1. *Ab initio* first-principles calculations

The electronic band structure of the cubic antiperovskites A_3EO is determined by performing first-principles calculations with the Vienna *ab initio* package [33,34] using the projector augmented wave (PAW) method [35,36]. As an input for the DFT calculation we used the experimental crystal structure of Ref. [25]. The lattice constant for Ca$_3$PbO is 4.847 Å. For the exchange-correlation functional, we chose the generalized-gradient approximation of Perdew-Burke-Ernzerhof type [37]. The plane-wave basis is truncated with an energy cutoff of 400 eV. For the bulk calculation a $12 \times 12 \times 12$ k mesh is used. Spin-orbit coupling effects are also taken into account.

The DFT calculations show that near the Fermi energy E_F the valence bands mostly originate from Pb-p orbitals (p_x, p_y, and p_z), while the orbital character of the conduction bands near E_F is Ca-$d_{x^2-y^2}$, Ca-d_{xz}, and Ca-d_{yz} (from three

different Ca atoms). Guided by these findings, we use these 12 orbitals (24 including spin) as a basis set to derive a low-energy tight-binding model. We determine the hopping parameter values for this tight-binding model from a maximally localized Wannier function (MLWF) method [38,39]. With this model, we compute the momentum-resolved surface density of states by means of an iterative Green's function method [40]. The results of these calculations are shown in Figs. 2–5. To determine the topological characteristics of Ca$_3$PbO, we have also used a simplified nine-band (18 bands including spin) tight-binding model, see Appendix B for details.

2. Topological invariants

The type-I and type-II Dirac surface states of the cubic antiperovskites are protected by a mirror Chern number. The mirror Chern number is defined as a two-dimensional integral over the reflection plane of the occupied wave functions with mirror eigenvalue $R = +1$ (or $R = -1$) [6,10]. Note that since the Hamiltonian H commutes with the reflection operator, the eigenfunctions of H can be assigned a definite mirror eigenvalue. Without loss of generality, one usually assumes that the mirror eigenvalues are ± 1, since $R^2 = 1$ after a suitable $U(1)$ gauge transformation [7]. The value of the mirror Chern number corresponds to the number of left- and right-moving chiral surface modes. These chiral surface modes exist within the mirror line of the surface BZ, i.e., within the line that is obtained by projecting the bulk mirror plane onto the surface BZ.

We have numerically computed the mirror Chern number using two different methods: (i) using the simplified tight-binding model of Appendix B and (ii) using the real space wave functions of the DFT-derived 12-band tight-binding model. For method (i), the reflection operator R can be written explicitly in momentum space. The momentum space Hamiltonian can then be block diagonalized with respect to R and the eigenfunctions can be obtained for each block separately (see Appendix B for details). For method (ii), the real-space wave functions of the 12-band tight-binding model are projected onto the mirror eigenspaces $(\mathbb{1} \pm R)/2$. This is done by identifying mirror-reflected orbitals with proper sign changes. Using these projected wave functions, a Fourier transform is performed along the two surface momenta to obtain the surface spectrum for a given reflection eigenspace. The Chern number can then be inferred from the number of chiral surface modes in the surface spectrum. Both methods (i) and (ii) agree with each other.

APPENDIX B: SIMPLIFIED TIGHT-BINDING MODEL OF Ca$_3$PbO

To construct a simplified tight-binding model we follow along the lines of the work by Kariyado and Ogata [22]. In Ref. [22], a six-band model with the orbitals

$$Pb_{p_x}, Pb_{p_y}, Pb_{p_z}, Ca^1_{d_{y^2-z^2}}, Ca^2_{d_{z^2-x^2}}, \text{and } Ca^3_{d_{x^2-y^2}}$$

was constructed. This six-band model exhibits six *gapless* Dirac nodes along the Γ-X direction, but does not contain a Dirac mass gap, which is present in the DFT calculations. To open up a gap, one needs to include in addition the

Ca^1-d_{yz}, Ca^2-d_{zx}, and Ca^3-d_{xy} orbitals. As we show below, the spin-orbit coupling between these orbitals and the Ca^1-$d_{y^2-z^2}$, Ca^2-$d_{z^2-x^2}$, and Ca^3-$d_{x^2-y^2}$ orbitals represents a mass term that opens up a gap at the six Dirac cones. We use this nine-band model to analyze the topological properties of Ca$_3$PbO (and other cubic antiperovskites) and to compute the mirror Chern numbers.

Thus, in the absence of spin-orbit coupling, our tight-binding Hamiltonian is written as $\mathcal{H} = \sum_{\mathbf{k}} \psi_{\mathbf{k}}^\dagger H_{k/2}(\mathbf{k}) \psi_{\mathbf{k}}$ with the nine-component spinor

$$\psi_{\mathbf{k}} = (Pb_{p_x}, \qquad Pb_{p_y}, \qquad Pb_{p_z},$$
$$Ca^1_{d_{y^2-z^2}}, \quad Ca^2_{d_{z^2-x^2}}, \quad Ca^3_{d_{x^2-y^2}},$$
$$Ca^1_{d_{yz}}, \qquad Ca^2_{d_{zx}}, \qquad Ca^3_{d_{xy}})^T$$

and the 9×9 matrix $H_{k/2}$, which can be expressed in block form as

$$H_{k/2}(\mathbf{k}) = \begin{pmatrix} H_p & V_{dp}^u & V_{dp}^l \\ V_{dp}^{u\,\dagger} & H_d^u & 0 \\ V_{dp}^{l\,\dagger} & 0 & H_d^l \end{pmatrix} \qquad (B1)$$

The blocks of $H_{k/2}(\mathbf{k})$ are given by

$$H_p = \begin{pmatrix} e_p - 2t_{pp}c_{2x} & 0 & 0 \\ 0 & e_p - 2t_{pp}c_{2y} & 0 \\ 0 & 0 & e_p - 2t_{pp}c_{2z} \end{pmatrix} \quad (B2)$$

and

$$H_d^u = \begin{pmatrix} e_d & -4t_{dd}c_x c_y & -4t_{dd}c_z c_x \\ -4t_{dd}c_x c_y & e_d & -4t_{dd}c_y c_z \\ -4t_{dd}c_z c_x & -4t_{dd}c_y c_z & e_d \end{pmatrix}$$

and $H_d^l = e_d \mathbb{1}_3$, with $\mathbb{1}_3$ the 3×3 identity matrix. The coupling terms between p and d orbitals are

$$V_{dp}^u = 4it_{pd} \begin{pmatrix} 0 & c_z s_x & -c_y s_x \\ -c_z s_y & 0 & c_x s_y \\ c_y s_z & -c_x s_z & 0 \end{pmatrix},$$

$$V_{dp}^l = 4it_{pd} \begin{pmatrix} 0 & c_x s_z & c_x s_y \\ c_y s_z & 0 & c_y s_x \\ c_z s_y & c_z s_x & 0 \end{pmatrix}, \qquad (B3)$$

where we have used the short-hand notation

$$c_i = \cos \frac{k_i}{2}, \quad s_i = \sin \frac{k_i}{2}, \quad c_{2i} = \cos k_i.$$

In order to simplify matters, we have neglected in the above expressions further neighbor hopping terms that were included in the work by Kariyado and Ogata [22]. We have checked that these simplifications do not alter the topological properties.

Let us now add spin-orbit coupling terms to the Hamiltonian (B1). The on-site spin-orbit coupling for the Pb-p orbitals is given by $\sum_{\mathbf{k}} \psi_p^\dagger(\mathbf{k}) H_{SO}^p(\mathbf{k}) \psi_p(\mathbf{k})$ with the spinor

$$\psi_p(\mathbf{k}) = (Pb_{p_x}^\uparrow, Pb_{p_y}^\uparrow, Pb_{p_z}^\uparrow, Pb_{p_x}^\downarrow, Pb_{p_y}^\downarrow, Pb_{p_z}^\downarrow)$$

and

$$H_{\text{SO}}^p(\mathbf{k}) = \frac{\lambda_p}{2} \begin{pmatrix} 0 & -i & 0 & 0 & 0 & 1 \\ i & 0 & 0 & 0 & 0 & -i \\ 0 & 0 & 0 & -1 & i & 0 \\ 0 & 0 & -1 & 0 & i & 0 \\ 0 & 0 & -i & -i & 0 & 0 \\ 1 & i & 0 & 0 & 0 & 0 \end{pmatrix}.$$

The on-site spin-orbit coupling for the d orbitals reads $\sum_{\mathbf{k}} \psi_d^\dagger(\mathbf{k}) H_{\text{SO}}^d(\mathbf{k}) \psi_d(\mathbf{k})$ with the spinor

$$\psi_d(\mathbf{k})$$
$$= (\text{Ca}_{d_{y^2-z^2}}^{1,\uparrow}, \text{Ca}_{d_{z^2-x^2}}^{2,\uparrow}, \text{Ca}_{d_{x^2-y^2}}^{3,\uparrow}, \text{Ca}_{d_{y^2-z^2}}^{1,\downarrow}, \text{Ca}_{d_{z^2-x^2}}^{2,\downarrow}, \text{Ca}_{d_{x^2-y^2}}^{3,\downarrow},$$
$$\text{Ca}_{d_{yz}}^{1,\uparrow}, \text{Ca}_{d_{zx}}^{2,\uparrow}, \text{Ca}_{d_{xy}}^{3,\uparrow}, \text{Ca}_{d_{yz}}^{1,\downarrow}, \text{Ca}_{d_{zx}}^{2,\downarrow}, \text{Ca}_{d_{xy}}^{3,\downarrow},)^T,$$

and

$$H_{\text{SO}}^d(\mathbf{k}) = \lambda_d \tau_y \otimes \left\{ \sigma_x \otimes \begin{pmatrix} 1 & 0 & 0 \\ 0 & 0 & 0 \\ 0 & 0 & 0 \end{pmatrix} \right.$$
$$\left. + \sigma_y \otimes \begin{pmatrix} 0 & 0 & 0 \\ 0 & 1 & 0 \\ 0 & 0 & 0 \end{pmatrix} + \sigma_z \otimes \begin{pmatrix} 0 & 0 & 0 \\ 0 & 0 & 0 \\ 0 & 0 & 1 \end{pmatrix} \right\}, \tag{B4}$$

where τ_β and σ_α represent d-orbital ($x_i^2 - x_j^2$ and $x_i x_j$) and spin (up and down) degree of freedom, respectively. As it turns out, $H_{\text{SO}}^d(\mathbf{k})$ gaps out the bulk Dirac cones.

Adding these spin-orbit coupling terms to Eq. (B1), we obtain the full Hamiltonian

$$H_{\text{tot}}^{k/2}(\mathbf{k}) = \begin{pmatrix} H_p^{\text{tot}}(\mathbf{k}) & V_{\text{tot}}(\mathbf{k}) \\ V_{\text{tot}}^\dagger(\mathbf{k}) & H_d^{\text{tot}}(\mathbf{k}) \end{pmatrix}, \tag{B5}$$

with

$$H_p^{\text{tot}}(\mathbf{k}) = \begin{pmatrix} H_p & 0 \\ 0 & H_p \end{pmatrix} + H_{\text{SO}}^p(\mathbf{k}),$$

$$H_d^{\text{tot}}(\mathbf{k}) = \begin{pmatrix} \sigma_0 \otimes H_d^u & 0 \\ 0 & \sigma_0 \otimes H_d^l \end{pmatrix} + H_{\text{SO}}^d(\mathbf{k}),$$

and

$$V_{\text{tot}}(\mathbf{k}) = \begin{pmatrix} \sigma_0 \otimes V_{dp}^u & \sigma_0 \otimes V_{dp}^l \end{pmatrix}.$$

Note that the outermost grading of H_p^{tot} and σ_0 in the above expressions corresponds to the spin grading. The parameters of the above tight-binding model can be determined by fitting to the DFT results. We have used the following values (in units of eV):

$$e_p = 0.0, \quad e_d = 2.0, \quad t_{pp} = -0.4,$$
$$t_{dd} = -0.4, \quad t_{pd} = -0.4, \quad \lambda_p = 0.75, \quad \lambda_d = 0.1.$$

We have checked that the nine-band model Hamiltonian (B5) exhibits qualitatively the same surface states as the DFT-derived twelve-band model (cf. Fig. 2).

Let us now compute the mirror Chern numbers for this model. To this end, we first need to determine the reflection operators. To remove fractional momenta in the symmetry

operators, we first perform a unitary transformation on the Hamiltonian (B5), i.e.,

$$H^k(\mathbf{k}) = U^\dagger H_{\text{tot}}^{k/2}(\mathbf{k}) U, \tag{B6}$$

where $U = \text{diag}(U^p, U^{d^u}, U^{d^l})$, with

$$U_p = e^{-i(k_x + k_y + k_z)/2} \mathbb{1}_6, \tag{B7}$$

$$U_d^u = U_d^l = \sigma_0 \otimes \begin{pmatrix} e^{-ik_x/2} & 0 & 0 \\ 0 & e^{-ik_y/2} & 0 \\ 0 & 0 & e^{-ik_z/2} \end{pmatrix}. \tag{B8}$$

The reflection operator R_x for the mirror symmetry $k_x \to -k_x$ is given by

$$U_{R_x}(\mathbf{k}) = \begin{pmatrix} R_x^p & 0 & 0 \\ 0 & R_x^{d^u} & 0 \\ 0 & 0 & R_x^{d^l} \end{pmatrix}, \tag{B9}$$

where

$$R_x^p = \sigma_x \otimes \begin{pmatrix} -1 & 0 & 0 \\ 0 & 1 & 0 \\ 0 & 0 & 1 \end{pmatrix},$$

$$R_x^{d^u} = \sigma_x \otimes \begin{pmatrix} 1 & 0 & 0 \\ 0 & e^{ik_x} & 0 \\ 0 & 0 & e^{ik_x} \end{pmatrix},$$

$$R_x^{d^l} = \sigma_x \otimes \begin{pmatrix} 1 & 0 & 0 \\ 0 & -e^{ik_x} & 0 \\ 0 & 0 & -e^{ik_x} \end{pmatrix}. \tag{B10}$$

The expression of the reflection operator $R_{x,-y}$ for the mirror symmetry $(k_x, k_y) \to (-k_y, -k_x)$ reads

$$U_{R_{x,-y}}(\mathbf{k}) = \begin{pmatrix} R_{x,-y}^p & 0 & 0 \\ 0 & R_{x,-y}^{d^u} & 0 \\ 0 & 0 & R_{x,-y}^{d^l} \end{pmatrix}, \tag{B11}$$

where

$$R_{x,-y}^p = -\frac{\sigma_x + \sigma_y}{\sqrt{2}} \otimes \begin{pmatrix} 0 & 1 & 0 \\ 1 & 0 & 0 \\ 0 & 0 & -1 \end{pmatrix},$$

$$R_{x,-y}^{d^u} = -\frac{\sigma_x + \sigma_y}{\sqrt{2}} \otimes \begin{pmatrix} 0 & e^{ik_x} & 0 \\ e^{ik_y} & 0 & 0 \\ 0 & 0 & e^{i(k_x+k_y)} \end{pmatrix},$$

$$R_{x,-y}^{d^l} = -\frac{\sigma_x + \sigma_y}{\sqrt{2}} \otimes \begin{pmatrix} 0 & e^{ik_x} & 0 \\ e^{ik_y} & 0 & 0 \\ 0 & 0 & -e^{i(k_x+k_y)} \end{pmatrix}. \tag{B12}$$

These two reflection symmetries act on the Hamiltonian (B6) as

$$H^k(\mathbf{k}) = U_{R_x}^\dagger H^k(-k_x, k_y, k_z) U_{R_x}, \tag{B13}$$

$$H^k(\mathbf{k}) = U_{R_{x,-y}}^\dagger H^k(-k_y, -k_x, k_z) U_{R_{x,-y}}. \tag{B14}$$

Due to these two mirror symmetries, the bulk wave functions of $H^k(\mathbf{k})$ in the mirror planes $k_x = 0$ and $k_x = -k_y$, respectively,

can be labeled by the mirror eigenvalues ± 1. Within these two-dimensional mirror planes in momentum space, one can compute the Chern number $n_{\pm 1}$ of the occupied bands for each mirror eigenvalue separately. The mirror Chern number is then given by $C = (n_{+1} - n_{-1})/2$. Using this approach we have computed the mirror Chern numbers for $H^k(\mathbf{k})$. We find that they are consistent with the number of chiral surface modes as computed from the DFT-derived twelve-band tight-binding model.

APPENDIX C: LOW-ENERGY EFFECTIVE THEORY

In this section, we study the topology of the cubic antiperovskites $A_3 E$O using a low-energy effective theory. As discussed in the main text, the surface states of $A_3 E$O are protected by the nine reflection symmetries

$$R_{k_x}\mathbf{k} = (-k_x, k_y, k_z), \quad R_{k_y, \pm k_z}\mathbf{k} = (k_x, \pm k_z, \pm k_y), \quad \text{(C1a)}$$

$$R_{k_y}\mathbf{k} = (k_x, -k_y, k_z), \quad R_{k_z, \pm k_x}\mathbf{k} = (\pm k_z, k_y, \pm k_x), \quad \text{(C1b)}$$

$$R_{k_z}\mathbf{k} = (k_x, k_y, -k_z), \quad R_{k_x, \pm k_y}\mathbf{k} = (\pm k_y, \pm k_x, k_z), \quad \text{(C1c)}$$

and the bulk band structure of $A_3 E$O exhibits six Dirac cones, which are gapped out by spin-orbit coupling. These six Dirac cones are located on the Γ-X high-symmetry lines of the bulk Brillouin zone, i.e., at

$$\mathbf{k} = (\pm\Delta, 0, 0),\ (0, \pm\Delta, 0),\ (0, 0\pm\Delta). \quad \text{(C2)}$$

In the absence of spin-orbit coupling, the low-energy physics near these six Dirac cones is described by the Hamiltonian [22]

$$H(\mathbf{k}) = \begin{cases} (k_x \pm \Delta)\sigma_x \otimes \sigma_z + k_y\sigma_y \otimes \sigma_z + k_z\sigma_z \otimes \sigma_z, & \text{near } \mathbf{k} = (\mp\Delta, 0, 0) \\ k_x\sigma_x \otimes \sigma_z + (k_y \pm \Delta)\sigma_y \otimes \sigma_z + k_z\sigma_z \otimes \sigma_z, & \text{near } \mathbf{k} = (0, \mp\Delta, 0) \\ k_x\sigma_x \otimes \sigma_z + k_y\sigma_y \otimes \sigma_z + (k_z \pm \Delta)\sigma_z \otimes \sigma_z, & \text{near } \mathbf{k} = (0, 0, \mp\Delta) \end{cases} \quad \text{(C3)}$$

We observe that Eq. (C3) is invariant under the nine mirror symmetries (C1). That is, the Hamiltonian $H(\mathbf{k})$ obeys

$$U_\#^{-1} H(\mathbf{k}) U_\# = H(R_\# \mathbf{k}) \quad \text{(C4)}$$

with the symmetry operators $U_{k_i} = \sigma_i \otimes \sigma_x$ and $U_{k_i, \pm k_j} = \frac{\sigma_i \mp \sigma_j}{\sqrt{2}} \otimes \sigma_x$. Moreover, we note that the six gapless Dirac cones of Eq. (C3) are located within the mirror planes $k_i = 0$ ($i = x, y, z$). Hence, in order to compute the mirror Chern number for these mirror planes, the Dirac nodes need to be gapped out, which occurs due to spin-orbit coupling. Within the low-energy model (C3), we find that there exists only one symmetry-preserving gap opening term, namely $m\mathbb{1} \otimes \sigma_x$, with m a constant that is independent of $\mathbf{k}$. The mass term $m\mathbb{1} \otimes \sigma_x$ gaps out all six Dirac nodes. As we will see, this turns the system into a nontrivial topological crystalline insulator. To show this, we need to determine the mirror Chern numbers.

Let us first consider the mirror Chern number in the $k_z = 0$ reflection plane. The eigenspace of U_{k_z} with mirror eigenvalue $+1$ is spanned by $|\psi_1\rangle = (1, 1, 0, 0)/\sqrt{2}$ and $|\psi_2\rangle = (0, 0, 1, -1)/\sqrt{2}$. Projecting the low-energy Hamiltonian (C3) within the reflection plane $k_z = 0$ onto this eigenspace gives

$$h(\mathbf{k})_{k_z} = \begin{cases} (k_x \pm \Delta)\sigma_x + k_y\sigma_y + m\sigma_z, & \text{near } (\mp\Delta, 0, 0), \\ k_x\sigma_x + (k_y \pm \Delta)\sigma_y + m\sigma_z, & \text{near } (0, \mp\Delta, 0). \end{cases} \quad \text{(C5)}$$

We observe that the four Dirac cones, which are located within the mirror plane $k_z = 0$ are gapped out by the same mass term $m\sigma_z$. Since all four Dirac cones have the same orientation, a sign change in m leads to a Chern number change by $+1$ for all of the four Dirac cones (or -1 for all the four Dirac cones). Hence the total mirror Chern number C_{z^0} changes by four, when $m \to -m$.

Second, we consider the mirror Chern number in the $k_x = -k_y$ reflection plane. The eigenspace of $U_{k_x, -k_y}$ with mirror eigenvalue $+1$ is spanned by the vectors $|\phi_1\rangle = (e^{-i\pi/8}, 0, 0, e^{i\pi/8})/\sqrt{2}$ and $|\phi_2\rangle = (0, e^{-i\pi/8}, e^{i\pi/8}, 0)/\sqrt{2}$. Projecting Hamiltonian (C3) within the reflection plane $k_x = -k_y$ onto this eigenspace yields

$$h(\mathbf{k})_{k_x, +k_y} = k_{xy}\sigma_y + (k_z \pm \Delta)\sigma_z + m\sigma_x, \quad \text{near } (0, 0, \mp\Delta), \quad \text{(C6)}$$

where $k_{xy} = (-k_x + k_y)/\sqrt{2}$. Because the two Dirac cones in Eq. (C6) have the same orientation, the total mirror Chern number $C_{x,y}$ changes by two, when $m \to -m$.

From these observations, we conclude that the total mirror Chern numbers are given by

$$C_{i^0} = 2\,\mathrm{sgn}(m) + b_i, \quad C_{i, \pm j} = \mathrm{sgn}(m) + b_{i, \pm j}, \quad \text{(C7)}$$

where b_i and $b_{i, \pm j}$ are the mirror Chern numbers of the "background" bands, i.e., those filled bands that are not included in the low-energy description (C3). We note that there exists the following relation between b_i and $b_{i, \pm j}$:

$$b_i - b_{i, \pm j} = 1 \bmod 2. \quad \text{(C8)}$$

This is because the number of chiral left- (or right-) moving surface modes on the $k_i = 0$ and $k_i = \pm k_j$ high symmetry lines can only differ by a multiple of two. That is, the surface modes on the $k_i = 0$ line are continuously connected to the surface modes on the $k_i = \pm k_j$ line. The only way how the number of chiral left- (or right-) moving modes can differ on these two high-symmetry lines is if left- (or right-) moving modes are gapped out pairwise.

Using the DFT-derived twelve-band tight-binding model and the simplified nine-band model, we find that $b_i = 0$ and $b_{i, \pm j} = 1$. Hence, $C_{i^0} = 2\,\mathrm{sgn}(m)$ and $C_{i, \pm j} = \mathrm{sgn}(m) + 1$, which is in agreement with the results of Ref. [26].

APPENDIX D: LANDAU LEVELS OF TILTED DIRAC CONES

In this appendix, we study the Landau level spectra of type-II Dirac surface states. We note that the Landau level structure of tilted Dirac fermions has been studied previously in the literature [32,41–47], in the context of strained graphene and certain organic conductors, like α-(BEDT $-$ TTF)$_2$I$_3$. We first review the properties of Landau level spectra of tilted type-I Dirac cones, and then extend these results to type-II Dirac surface states.

1. Effective model approach

We start by considering a toy model describing a tilted Dirac cone. The Hamiltonian of this model is given by

$$H_0 = v_F(\eta \pi_y \sigma_0 + \pi_x \sigma_x + \pi_y \sigma_y), \tag{D1}$$

where $\pi_i = \hbar k_i + eA_i$ denotes the canonical momentum, σ_i are the Pauli matrices, and η parametrizes the degree of tilting along the k_y direction. For $\eta < 1$ ($\eta > 1$), Eq. (D1) describes a type-I (type-II) Dirac cone with an energy dispersion as shown in Fig. 7.

The Landau level spectrum of the above Hamiltonian can be obtained in a closed form when $0 \leqslant \eta < 1$, which shows that quantized Landau levels exist for all type-I Dirac cones. Specifically, if we adopt the Landau gauge $A = (0, Bx)$, the spectrum of H_0 reads [45]

$$E_n = \text{sgn}(n)\sqrt{2eB\hbar v_F^2 |n| \lambda^3}, \tag{D2}$$

where $\lambda = \sqrt{1 - \eta^2}$, and n is the Landau level index. One intuitive way to understand why Landau level-like spectra still persists for a tilted Dirac cone with $0 \leqslant \eta < 1$ is that all constant-energy contours in the momentum space are still closed loops, although with an anisotropic shape [48]. As a result, quantized Landau levels can be derived within a semiclassical picture [49]. Mathematically, the reason for the existence of quantized Landau levels is that the corresponding eigenvalue problem $H_0\Phi(r) = E\Phi(r)$ can be mapped to the problem of a one-dimensional harmonic oscillator, as long as $0 \leqslant \eta < 1$. Specifically, the eigenstates are governed by the following differential equation [45],

$$\left[-\frac{d^2}{dX^2} + (1-\eta^2)\left(X + \frac{\eta}{1-\eta^2}\varepsilon\right)^2 \right]\phi(X)$$

$$= \begin{pmatrix} \frac{\varepsilon^2}{1-\eta^2} - 1 & i\eta \\ i\eta & \frac{\varepsilon^2}{1-\eta^2} + 1 \end{pmatrix}\phi(X), \tag{D3}$$

where $\varepsilon = E\ell_B/(\hbar v_F)$, $X = x/\ell_B + k_y\ell_B$, with k_y being the conserved momentum in the Landau gauge, and $\ell_B = \sqrt{\hbar/(eB)}$ is the magnetic length. Because the coefficient of the second term is $1 - \eta^2 > 0$, harmonic oscillator states are valid solutions of the above eigenvalue problem, as long as $\eta < 1$.

The above discussion also makes it clear that Landau level-like spectra no longer exists if $\eta > 1$, as the coefficient of the second term in the differential equation (D3) becomes negative. Physically, this is because the constant-energy contours now become unbounded (cf. the solid lines in Fig. 7) in this effective model.

2. Tight-binding model approach

We now use a tight-binding model to illustrate how the Landau level spectra evolve as the Dirac cone is titled from a type-I cone to a type-II cone. Specifically, we adopt the following tight-binding model on the square lattice [32],

$$H = -\sum_{\langle ij \rangle} t_{ij} b_j^\dagger a_i + t_1 \sum_{\langle ij \rangle} (a_j^\dagger a_i + b_j^\dagger b_i), \tag{D4}$$

where the operator a_i (b_i) annihilates an electron on site A_i (B_i). The next-nearest-neighbor hopping parameters along the dashed bonds in Fig. 8 are given by t_1, while the nearest-neighbor hopping amplitude t_{ij} are specified as $t_a = t_b = t_c = -t$, $t_d = t$. In the following, we will calculate the spectrum of (D4) in a ribbon geometry, as shown by the gray rectangle in Fig. 8, which is periodic along the k_2 direction and finite along k_1.
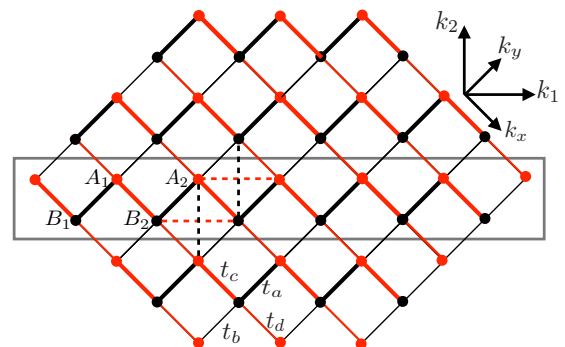
FIG. 8. Illustration of the square lattice, on which the tight-binding model (D4) is defined. The lattice is bipartite with each unit cell containing two inequivalent atoms labeled by A (red) and B (black). The second neighbor hopping integral along all dashed lines is t_1. The nearest-neighbor hopping is specified as $t_a = t_b = t_c = -t$, $t_d = t$. The gray rectangle marks the ribbon geometry in our calculation, which is periodic along the k_2 direction and finite along the k_1 direction.

FIG. 7. Comparison between a type-I (dashed lines) and a type-II (solid lines) Dirac fermion. Shown are the energy dispersions of Eq. (D1) with $\eta = 0.5$ (type-I) and $\eta = 2$ (type-II). The valence bands are marked by yellow and light blue for type-I and type-II Dirac fermions, respectively.

The energy bands of Hamiltonian (D4) in ribbon geometry are shown in Fig. 6 of the main text. The degree of tilting of the two Dirac cones is controlled by the ratio t_1/t. Specifically, when $t_1/t = 0$ there is no tilting [Fig. 6(a)]; when t_1/t starts to increase, the two Dirac cones begin to tilt [Fig. 6(b)]; when $t_1/t = 1/2$ the spectrum is nondispersive along the k_2 direction [Fig. 6(c)]; finally, when $t_1/t > 1/2$, type-II Dirac cones appear [Fig. 6(d)].

Such a transition from a type-I to a type-II Dirac cone also manifests itself in a drastic change in the Landau level structure, which can be obtained by the Peierls substitution as follows. We adopt the Landau gauge and write the vector potential as $A = (0, Bx)$, which will attach a phase factor for all hopping processes in the tight-binding model in Eq. (D4). Specifically, for a hopping from lattice point (x_i, y_i) to (x_f, y_f), the associated phase factor will be $e^{i\theta}$, with

$$\theta = \frac{e}{\hbar} \int_C A \cdot dr = \frac{(x_f + x_i)(y_f - y_i)}{2\ell_B^2}. \qquad \text{(D5)}$$

Figure 6 shows the corresponding Landau level spectrum when $\lambda \equiv Ba^2/\phi_0 = 0.01$. We can see that when $t_1/t < 0.5$, well separated Landau levels exist around the Dirac node, although the level spacing decreases as t_1 increases [Figs. 6(a) and 6(b)]. In contrast, when the transition to a type-II Dirac cone occurs, the spacing of the Landau level around the node becomes extremely small; the Landau levels with finite separation are due to the contributions from other parts of the band structure [Figs. 6(c) and 6(d)].

The change in the Landau level structure stems from a change in the Fermi surface topology. In fact, it is generally expected that a large Fermi surface area is associated with dense Landau levels. One simple example is type-I Dirac cones with different Fermi velocities: for a given energy, the one with a smaller (larger) Fermi velocity has a larger (smaller) Fermi surface area, which is also associated with a small (large) Landau level spacing. One can also gain an intuitive understanding of this from a semiclassical point of view [49,50]. We first note that the Landau levels will occur whenever the semiclassical orbits of electrons in **k** space encloses some critical areas specified by the following condition [49]

$$\frac{\hat{B}}{2} \cdot \oint_{C_m} \mathbf{k}_c \times d\mathbf{k}_c = 2\pi \left(m + \frac{1}{2} - \frac{\Gamma_{C_m}}{2\pi} \right) \frac{eB}{\hbar}, \qquad \text{(D6)}$$

where C_m is the mth semiclassical orbit of the electron, and Γ_{C_m} is the Berry phase of this energy contour. We thus see

that an additional Landau level will be formed whenever the area of the **k**-space semiclassical orbit increases by $2\pi eB/\hbar$. In particular, note that this increment is independent of the Landau level index m. We can now explain why a large Fermi surface is usually associated with dense Landau levels: a large Fermi surface indicates a semiclassical orbit with a large circumference, and thus a small change in the semiclassical orbit size $|\Delta \mathbf{k}_c|$ is sufficient to reach the next critical area. As a result, as long as the Fermi velocity is not extremely large, we should expect only a small change in the Landau level energy. Therefore a large Fermi surface area is usually associated with dense Landau levels.

3. Relation to the (111) surface states

We now discuss the Landau level structure for the (111) surface states of the antiperovskite Ca$_3$PbO. As shown in Fig. 4(b) of the main text, the characteristics of the spectrum on the (111) surface is that two type-I Dirac nodes are located at the $\bar{\Gamma}$ point and that their energies are higher than the type-II Dirac nodes away from the $\bar{\Gamma}$ point. To describe this surface spectrum we consider the following effective model:

$$H_{\mathbf{k}}/t = \begin{pmatrix} \epsilon_a(\mathbf{k}) & \gamma_{\mathbf{k}} & T_{\mathbf{k}} & 0 \\ \gamma_{\mathbf{k}}^\dagger & \epsilon_b(\mathbf{k}) & 0 & T_{\mathbf{k}} \\ T_{\mathbf{k}} & 0 & \epsilon_c(\mathbf{k}) & \gamma_{\mathbf{k}} \\ 0 & T_{\mathbf{k}} & \gamma_{\mathbf{k}}^\dagger & \epsilon_d(\mathbf{k}) \end{pmatrix}, \qquad \text{(D7)}$$

where t is an overall energy multiplier and

$$\epsilon_\alpha(\mathbf{k}) = W_\alpha[\cos(ak_x) + \cos(ak_y)] + M_\alpha, \ \alpha = a,b,c,d. \qquad \text{(D8)}$$

Here, a is the distance $|A_1 B_1|$ in Fig. 8. Moreover, we have $\gamma_{\mathbf{k}} = \sin(ak_x) - i \sin(ak_y)$, and $T_{\mathbf{k}} = v_2 \sin(ak_x) \sin(ak_y)$. For the numerical evaluations, we choose the parameters as $(W_a, M_a) = (2.58, -0.50)$, $(W_b, M_b) = (-0.42, 5.50)$, $(W_c, M_c) = (1.16, 0)$, $(W_d, M_d) = (3.16, -4.00)$, and $v_2 = 0.25$, respectively. The energy spectrum of this model at $k_1 = 0$ is shown in Fig. 9(a), which captures the Dirac features of the (111) surface state [cf. Fig. 4(b) in the main text]. We note that this effective model possesses a C_3 rotation symmetry, instead of the C_4 rotation symmetry in the actual (111) surface of the antiperovskites; hence, there are four type-II Dirac nodes, instead of six.

In order to calculate the Landau level spectrum of this model, we assume that it is defined on the square lattice
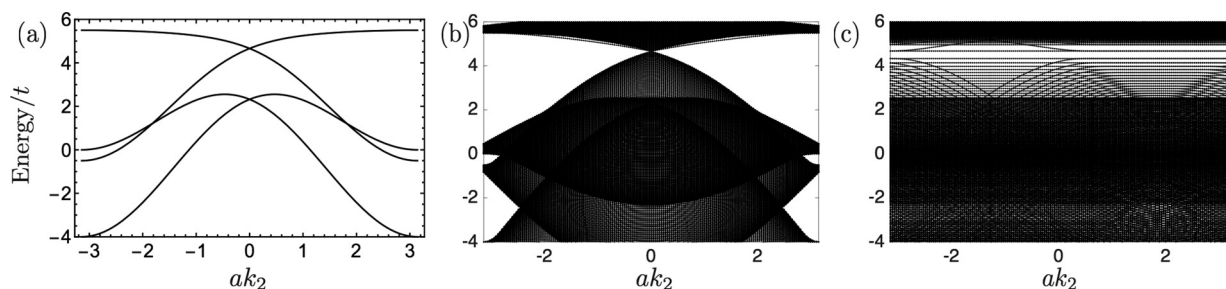
FIG. 9. (a) Bulk energy spectrum of model (D7) as a function ok k_2 with $k_1 = 0$. (b) Energy spectrum of Hamiltonian (D7) in a ribbon geometry with the edges along the k_2 direction. (c) Landau level spectrum of Hamiltonian (D7) with $\lambda \equiv Ba^2/\phi_0 = 0.05$. We note that all dispersive curves in the Landau level structure arise from states localized at the edge of the ribbon.

(a)   (b)
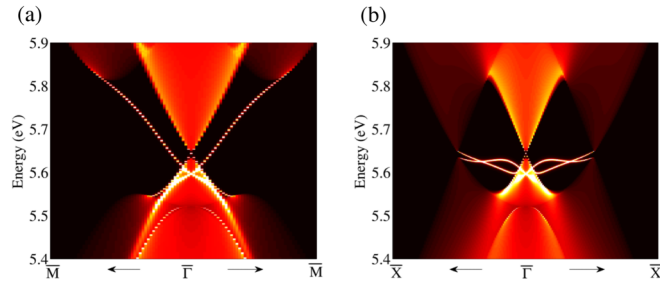
FIG. 10. Surface density of states along the high-symmetry lines (a) $\bar{\Gamma} \to \bar{X}$ and (b) $\bar{\Gamma} \to \bar{M}$ of the (001) surface BZ for the Ca-O termination [lower right panel of Fig. 1(b)]. In both the plots, a small surface band crossing, which is barely visible, is located at the bulk gap of $\bar{\Gamma}$ point.

shown in Fig. 8, where each site now hosts four orbitals $(A_{\mathbf{k}}, B_{\mathbf{k}}, C_{\mathbf{k}}, D_{\mathbf{k}})$, which constitutes the basis of the Hamiltonian $H_{\mathbf{k}}$, Eq. (D7). For convenience, we also make a coordinate transformation, namely $k_1 = k_x + k_y$, and $k_2 = k_x - k_y$. We then keep the system periodic along the k_2 direction, while finite along the k_1 direction. In particular, we only retain the lattice points marked by the gray rectangle in Fig. 8. The energy spectrum of such a ribbon geometry is shown in Fig. 9(b). The Landau level spectrum of (D7) for $\phi/\phi_0 = 0.05$ is shown in Fig. 9(c). The type-I and type-II Dirac nodes exhibit distinguishable physical features. Near the type-I Dirac node at $E/t \sim 4.5$, Landau levels are well separated since only a single Fermi surface appears near the node. Near the type-II Dirac nodes and the second type-I Dirac node at $E/t \sim 1.5$, on the other hand, the spacing of the Landau levels is close to zero due to the complexity of the Fermi surface structures.

APPENDIX E: SURFACE STATES FOR THE OTHER TERMINATION

For completeness we show in this section the surface states for the other surface terminations. Figure 10 displays the Dirac

(a)   (b)
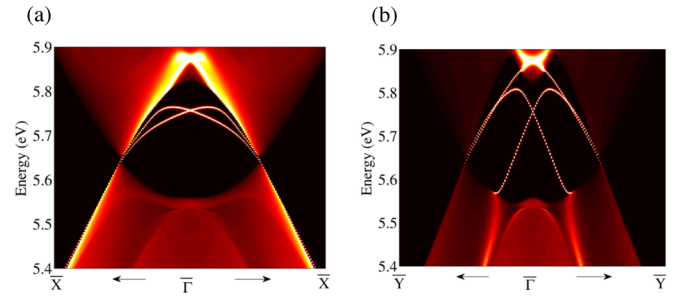
FIG. 11. Surface density of states along the high-symmetry lines (a) $\bar{\Gamma} \to \bar{X}$ and (b) $\bar{\Gamma} \to \bar{Y}$ of the (011) surface BZ for the Ca termination.

states on the (001) surface for the Ca-O termination. The surface density of states is plotted along the high-symmetry lines $\bar{\Gamma} \to \bar{X}$ and $\bar{\Gamma} \to \bar{M}$, corresponding to the $k_x = 0$ and $k_x = k_y$ mirror lines, respectively. Both in Figs. 10(a) and 10(b), two chiral left- and right-moving surface states are visible, which connect valence with conduction bands. This is in agreement with the mirror Chern numbers C_{x^0} and $C_{x,y}$ which take the value 2. In Fig. 10(a), there is in addition a trivial surface state which intersects with one of the left-(right-)moving chiral modes.

Figure 11 shows the Dirac states on the (011) surface for the Ca termination. The surface density of states is plotted along the high-symmetry lines $\bar{\Gamma} \to \bar{X}$ and $\bar{\Gamma} \to \bar{Y}$, which corresponds to the $k_x = 0$ and $k_y = k_z$ mirror lines, respectively. Since $C_{x^0} = C_{y,z} = 2$ there appear two left- and two right-moving chiral modes. In Fig. 11(b) the chiral modes form a type-II Dirac corssing.

In closing, we note that within our twelve-band tight-binding description the (111) surface spectrum with O termination is identical to the one with Ca-Pb termination. This is because our tight-binding model does not include oxygen orbitals, since they are far away in energy from E_F.

[1] X.-L. Qi and S.-C. Zhang, Rev. Mod. Phys. **83**, 1057 (2010).

[2] M. Z. Hasan and C. L. Kane, Rev. Mod. Phys. **82**, 3045 (2010).

[3] A. Bansil, H. Lin, and T. Das, Rev. Mod. Phys. **88**, 021004 (2016).

[4] C.-K. Chiu, J. C. Y. Teo, A. P. Schnyder, and S. Ryu, Rev. Mod. Phys. **88**, 035005 (2016).

[5] Y. Ando and L. Fu, Annu. Rev. Condens. Matter Phys. **6**, 361 (2015).

[6] J. C. Y. Teo, L. Fu, and C. L. Kane, Phys. Rev. B **78**, 045426 (2008).

[7] C.-K. Chiu, H. Yao, and S. Ryu, Phys. Rev. B **88**, 075142 (2013).

[8] T. Morimoto and A. Furusaki, Phys. Rev. B **88**, 125129 (2013).

[9] K. Shiozaki and M. Sato, Phys. Rev. B **90**, 165114 (2014).

[10] T. H. Hsieh, H. Lin, J. Liu, W. Duan, A. Bansil, and L. Fu, Nat. Commun. **3**, 982 (2012).

[11] P. Dziawa, B. J. Kowalski, K. Dybko, R. Buczko, A. Szczerbakow, M. Szot, E. Łusakowska, T. Balasubramanian,

B. M. Wojek, M. H. Berntsen, O. Tjernberg, and T. Story, Nat. Mater. **11**, 1023 (2012).

[12] Y. Tanaka, Z. Ren, T. Sato, K. Nakayama, S. Souma, T. Takahashi, K. Segawa, and Y. Ando, Nat. Phys. **8**, 800 (2012).

[13] S.-Y. Xu, C. Liu, N. Alidoust, M. Neupane, D. Qian, I. Belopolski, J. D. Denlinger, Y. J. Wang, H. Lin, L. A. Wray, G. Landolt, B. Slomski, J. H. Dil, A. Marcinkova, E. Morosan, Q. Gibson, R. Sankar, F. C. Chou, R. J. Cava, A. Bansil, and M. Z. Hasan, Nat. Commun. **3**, 1192 (2012).

[14] We note that in TCIs the type of the Dirac surface state is not dictated by the bulk topology. That is, type-II Dirac surface states can be adiabatically transformed into type-I surface states without changing the bulk topology. However, in conventional topological insulators the surface states must be of type-I due to time-reversal symmetry, see Sec. II.

[15] A. A. Soluyanov, D. Gresch, Z. Wang, Q. Wu, M. Troyer, X. Dai, and B. A. Bernevig, Nature (London) **527**, 495 (2015).

[16] Y. Xu, F. Zhang, and C. Zhang, Phys. Rev. Lett. **115**, 265304 (2015).

[17] L. Muechler, A. Alexandradinata, T. Neupert, and R. Car, Phys. Rev. X **6**, 041069 (2016).

[18] C. Wang, Y. Zhang, J. Huang, S. Nie, G. Liu, A. Liang, Y. Zhang, B. Shen, J. Liu, C. Hu, Y. Ding, D. Liu, Y. Hu, S. He, L. Zhao, L. Yu, J. Hu, J. Wei, Z. Mao, Y. Shi, X. Jia, F. Zhang, S. Zhang, F. Yang, Z. Wang, Q. Peng, H. Weng, X. Dai, Z. Fang, Z. Xu, C. Chen, and X. J. Zhou, Phys. Rev. B **94**, 241119(R) (2016).

[19] Y. Wu, D. Mou, N. H. Jo, K. Sun, L. Huang, S. L. Bud'ko, P. C. Canfield, and A. Kaminski, Phys. Rev. B **94**, 121113(R) (2016).

[20] S.-Y. Xu, N. Alidoust, G. Chang, H. Lu, B. Singh, I. Belopolski, D. Sanchez, X. Zhang, G. Bian, H. Zheng, M.-A. Husanu, Y. Bian, S.-M. Huang, C.-H. Hsu, T.-R. Chang, H.-T. Jeng, A. Bansil, V. N. Strocov, H. Lin, S. Jia, and M. Zahid Hasan, arXiv:1603.07318.

[21] T. Kariyado and M. Ogata, J. Phys. Soc. Jpn. **80**, 083704 (2011).

[22] T. Kariyado and M. Ogata, J. Phys. Soc. Jpn. **81**, 064701 (2012).

[23] Y. Fuseya, M. Ogata, and H. Fukuyama, J. Phys. Soc. Jpn. **81**, 013704 (2012).

[24] T. Kariyado, Three-dimensional dirac electron systems in the family of inverse-perovskite material Ca_3PbO, Ph.D. thesis, The University of Tokyo, Tokyo, 2012.

[25] J. Nuss, C. Mühle, K. Hayama, V. Abdolazimi, and H. Takagi, Acta Crystallographica Sec. B **71**, 300 (2015).

[26] T. H. Hsieh, J. Liu, and L. Fu, Phys. Rev. B **90**, 081112 (2014).

[27] M. Oudah, A. Ikeda, J. N. Hausmann, S. Yonezawa, T. Fukumoto, S. Kobayashi, M. Sato, and Y. Maeno, Nat. Commun. **7**, 13617 (2016).

[28] In Eq. (2.1), we have neglected a k-independent mass term $m\sigma_0$, since this term only results in a shift in the Fermi energy.

[29] C.-K. Chiu and A. P. Schnyder, Phys. Rev. B **90**, 205136 (2014).

[30] X.-Y. Dong and C.-X. Liu, Phys. Rev. B **93**, 045429 (2016).

[31] C. Fang, M. J. Gilbert, and B. A. Bernevig, Phys. Rev. Lett. **112**, 106401 (2014).

[32] T. Kawarabayashi, Y. Hatsugai, T. Morimoto, and H. Aoki, Phys. Rev. B **83**, 153414 (2011).

[33] G. Kresse and J. Furthmüller, Phys. Rev. B **54**, 11169 (1996).

[34] G. Kresse and J. Furthmüller, Comput. Mater. Sci. **6**, 15 (1996).

[35] P. E. Blöchl, Phys. Rev. B **50**, 17953 (1994).

[36] G. Kresse and D. Joubert, Phys. Rev. B **59**, 1758 (1999).

[37] J. P. Perdew, K. Burke, and M. Ernzerhof, Phys. Rev. Lett. **77**, 3865 (1996).

[38] A. A. Mostofi, J. R. Yates, Y.-S. Lee, I. Souza, D. Vanderbilt, and N. Marzari, Comput. Phys. Commun. **178**, 685 (2008).

[39] N. Marzari, A. A. Mostofi, J. R. Yates, I. Souza, and D. Vanderbilt, Rev. Mod. Phys. **84**, 1419 (2012).

[40] M. P. L. Sancho, J. M. L. Sancho, J. M. L. Sancho, and J. Rubio, J. Phys. F **15**, 851 (1985).

[41] A. Kobayashi, S. Katayama, Y. Suzumura, and H. Fukuyama, J. Phys. Soc. Jpn. **76**, 1 (2007).

[42] M. O. Goerbig, J.-N. Fuchs, G. Montambaux, and F. Piéchon, Phys. Rev. B **78**, 045415 (2008).

[43] T. Morinari, T. Himura, and T. Tohyama, J. Phys. Soc. Jpn. **78**, 023704 (2009).

[44] M. O. Goerbig, J.-N. Fuchs, G. Montambaux, and F. Piéchon, Euro. Phys. Lett. **85**, 57005 (2009).

[45] T. Morinari and T. Tohyama, J. Phys. Soc. Jpn. **79**, 044708 (2010).

[46] Y. Hatsugai, T. Kawarabayashi, and H. Aoki, Phys. Rev. B **91**, 085112 (2015).

[47] I. Proskurin, M. Ogata, and Y. Suzumura, Phys. Rev. B **91**, 195413 (2015).

[48] X. Li, F. Zhang, and A. H. MacDonald, Phys. Rev. Lett. **116**, 026803 (2016).

[49] D. Xiao, Q. Niu, and M.-C. Chang, Rev. Mod. Phys. **82**, 1959 (2010).

[50] Y. Gao and Q. Niu, arXiv:1507.06342.